Outdoor BLAST Measurement System at 2.44 GHz: Calibration and Initial Results

Michael J. Gans, *Fellow, IEEE*, Noach Amitay, *Life Fellow, IEEE*, Yu Shuan (Albert) Yeh, *Fellow, IEEE*, Hao Xu, *Member, IEEE*, T. C. Damen, Reinaldo A. Valenzuela, *Fellow, IEEE*, Theodore Sizer, *Member, IEEE*, R. Storz, D. Taylor, W. M. MacDonald, Cuong Tran, and Andrew Adamiecki

***Abstract*—There are ever increasing demands for additional capacity in wireless communications to handle voice, data, and wideband Internet applications. These demands are constrained by the bandwidth that was allocated to wireless communications. The spectral efficiencies in present day wireless systems hover around 1 bit/s/Hz. Bell-labs Layered Space–Time (BLAST) is a communication technique for achieving very high spectral efficiencies in highly scattering environments using multiple transmit and receive antennas. A measurement campaign was undertaken to assess the BLAST gains in spectral efficiency in the suburban outdoor environment for stationary subscribers. The measurements employed directive antennas to better control interference from adjacent cells. The measurements were performed over a narrow band at 2.44 GHz with five transmitting and seven receiving antennas, respectively. Extensive calibration methods, assisted by simulations, were developed to assure accurate results for the BLAST capacities of the measured remote subscriber sites.**

Initial results indicate that BLAST capacities of $C_B \geq$ 38 bits/s/Hz at 20% of the measured locations and $C_B \geq$ 24 bits/s/Hz at 50% of these locations are feasible, for reasonable link parameters and negligible interference.

***Index Terms*—BLAST, channel capacity, fixed wireless systems, measurements, MIMO channels.**

I. Introduction

A NOVEL concept to substantially increase the spectral efficiency in highly scattering environments, named Bell-labs Layered Space–Time (BLAST), was introduced by Foschini [1], [2]. Multiple receive and transmit antennas are utilized in this novel approach. The amount of increase in channel spectral efficiency is related to the randomness of the wireless environment produced by scattering, diffraction and reflection of the propagating electromagnetic waves. The actual performance of the BLAST technology depends on the detailed knowledge of the space–time channel.

Numerous spatial channel models have been developed in recent years due to the increasing interests in adaptive antennas, space-time coding, and other advanced space-time receiver techniques such as BLAST [3]–[7]. Measurement programs to determine the potential BLAST capacities in various propagation media and environments are in progress. Initial measurement results for BLAST technology have demonstrated high spectral efficiency for indoor propagation environments [10], [11], outdoor-to-indoor environment [9], and outdoor environment [8]. In [10] and [11], spectral efficiency ranged from 20 to 40 bits/s/Hz at signal-to-noise ratio (SNR) of 24–34 dB for a system with eight transmit antennas and 12 receive antennas. In [9], results show 27.9 bits/s/Hz for uncorrelated environment and 17 bits/s/Hz for correlated environment at a SNR of 30 dB in the case of a 4 transmit $\times$ 4 receive antennas set-up. In [8], capacity was measured with a 4×4 antenna system, and compared with the capacity of a single antenna system. Results show that the capacity of a 4×4 system is close to four times of the capacity of a single antenna system. In all these measurement campaigns, omnidirectional or sector antennas were used at the receiver.

The possible degradation of the spectral efficiency of BLAST systems with the use of highly directive antennas has yet to be determined. The choice of antennas' directivity is a compromise between interference control and link budget improvements versus reduction of the randomness of the wireless communications channel. The measurement campaign discussed here addresses the suburban outdoor environment for stationary subscribers when highly directive antennas are employed to better control interference from other cells.

Our narrowband measurements are performed at 2.44 GHz with $N_T = 5$ transmitting and $N_R = 7$ receiving antennas, respectively. Each transmitter is labeled by a different continuous-wave transmitted frequency. These frequencies are 2.44 GHz + (8, 9, 10, 11, 12 kHz). All these frequencies are simultaneously received at the seven receivers, downconverted, digitized, and Fourier transformed. The results are the transfer coefficients between every possible combination of receive–transmit antenna pairs. These coefficients are arranged in a 5×7 matrix $\mathbf{G}$, called the transfer matrix. The $\mathbf{H}$ matrix is obtained by the normalization of $\mathbf{G}$, as outlined in [1] and [2]

$$\mathbf{H} = \frac{\mathbf{G}}{\sqrt{\frac{\sum_{\forall(m,n)} |G(m,n)|^2}{N_T N_R}}}. \tag{1a}$$

Manuscript received March 23, 2001; revised October 17, 2001. This paper was presented in part at the IEEE VTC, Rhodes, Greece, May 6–9, 2001.

M. J. Gans, H. Xu, R. A. Valenzuela, T. Sizer, C. Tran, and A. Adamiecki are with Bell Laboratories, Holmdel, NJ 07733 USA (e-mail: haoxu@lucent.com).

N. Amitay, retired, was with the Wireless Communications Systems Department, AT&T Bell Laboratories, Holmdel, NJ 07733 USA.

Y. S. Yeh, retired, was with AT&T Bell Laboratories, Holmdel, NJ. He is now with Sigma Management, Freehold, NJ.

W. M. MacDonald is with Bell Laboratories, Murray Hill, NJ 07974-0636 USA.

Publisher Item Identifier S 0733-8716(02)03298-5.

This $\mathbf{H}$ matrix is utilized in evaluating the potential BLAST capacity [1], [2], C_B, of the transmit-to-receive channel, given by

$$C_B = \log_2 \left\{ \det \left| \mathbf{I} + \left(\frac{\rho}{N_T} \right) \mathbf{H}^\dagger \mathbf{H} \right| \right\} \text{ in bits/s/Hz} \quad (1b)$$

where ρ is a *projected* average communications system SNR,[1] $\det |\mathbf{X}|$ designates the determinant of a matrix $\mathbf{X}$, $\mathbf{H}^\dagger\mathbf{H}$ is the matrix product of the Hermitian of $\mathbf{H}$ and $\mathbf{H}$ while $\mathbf{I}$ is an identity matrix having the same dimension as $\mathbf{H}^\dagger\mathbf{H}$; i.e., N_T by N_T. It can be shown, with the aid of a unitary transformation, that C_B can be expressed as

$$C_B = \log_2 \left\{ \det \left| \mathbf{I} + \left(\frac{\rho}{N_T} \right) \mathbf{\Lambda} \right| \right\} \text{ in bits/s/Hz.} \quad (2)$$

$\mathbf{\Lambda}$ being the diagonal matrix of the eigenvalues, $\{\lambda_i\}$, of $\mathbf{H}^\dagger\mathbf{H}$. Thus, (2) can be rewritten as

$$C_B = \log_2 \left\{ \prod_{i=1}^{N_T} \left[1 + \left(\frac{\rho}{N_T} \right) \lambda_i \right] \right\}. \quad (3)$$

Measurement system noise and equipment nonlinearity could influence the accuracy of H and thereby C_B. The measured accuracy of C_B associated with environmental "keyholes" [12], [15] is most susceptible to errors due to the noise and nonlinearities. A keyhole channel refers to the channel with only one nonzero eigenvalue for $\mathbf{H}$, therefore, the channel capacity is minimum. An important sensitive parameter to detect measurement errors is defined as the number of degrees of freedom, D_F, which differs from the one defined in [13]. It is related to the rank of the matrix $\mathbf{H}^\dagger\mathbf{H}$ and is given by

$$D_F = C_B|_\rho - C_B|_{\rho/2}, \text{ with } \rho = 1000. \quad (4)$$

Although D_F varies slowly with ρ, we chose to fix ρ to be 1000 as part of the definition. When ρ is sufficiently large, all the eigenvalues, even the small ones, contribute to the total capacity, so that D_F is given by

$$D_F \approx \log_2 \frac{\prod_{i=1}^{N_T} \left[\left(\frac{\rho}{N_T} \right) \right]}{\prod_{i=1}^{N_T} \left[\left(\frac{\rho}{2N_T} \right) \right]} = \log_2 \left(2^{N_T} \right) = N_T; \quad \text{for } \left(\frac{\rho}{N_T} \right) \lambda_i \gg 1 \text{ and } \forall\, i \quad (5)$$

where N_T is the upper bound of D_F. For other λ_i's and especially those that are sufficiently small, i.e., $(\rho/N_T)\lambda_i \ll 1$, (3) and (4) clearly show that D_F is less than N_T.

The measurement system is described in Section II. System simulations, careful calibration, and measurements procedures are presented in Sections III–V, respectively. Processed results of our initial measurements are highlighted in Section VI with conclusions in Section VII.

[1]The projected system SNR is the SNR at each receiver antenna when total power is radiated from a single transmitter and averaged over all transmitter-receiver combinations.

Fig. 1. BLAST measurements apparatus.

II. Measurement System

Our measurement system consists of $N_T = 5$ transmitting base station antennas and $N_R = 7$ receiving remote antennas. The five transmitting antennas are horizontally arranged and uniformly spaced by 0.52 m. They are mounted on a turntable on top of a 35-m-high stationary mast located on top of Crawford Hill (65.5 m above the average surrounding terrain). This turntable can rotate through 360° in azimuth and can be tilted down by as much as 20° in elevation. The mast is shown in Fig. 1 on the right. Each transmitting antenna has 64 elements, which results in the beamwidths of 15° in azimuth and elevation. The feed network for these 64 elements has loss, which reduces the gain to 13 dB. The seven receiving antennas are arranged in an asymmetric cross, Fig. 2, and mounted on a turntable on top of a pneumatically controlled mast. Each receiving antenna has 16 elements, which results in the beamwidths of 26° in azimuth and elevation. With consideration of the loss of the feed network, the antenna gain is 15 dB. The mast can extend to up to 10 m. It is anchored to the roof of a van as shown in Fig. 1. This van represents the remote subscriber. During the travel of the van from one location to another, the mast is retracted and the cross of antennas is folded.

A schematic diagram of the base station antenna transmitter is shown in Fig. 3. Each transmitting antenna is excited by a different frequency. A set of five frequencies is generated by five Analog Devices AD-9856 Direct Digital Synthesizers (DDS), as indicated in the figure. The external clocks of these

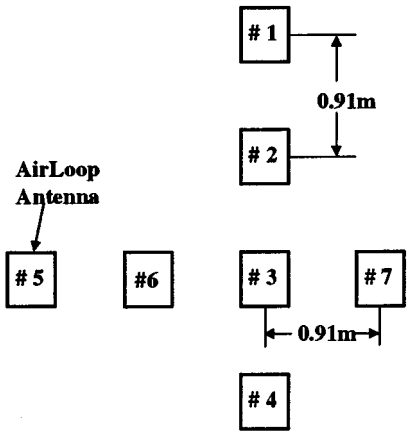

Fig. 2. Front view of asymmetric cross arrangement of the receiving antennas.

devices are derived from a single GPS-controlled Rubidium clock. These five low frequencies are cabled to the top of the base station and individually fed to five Nova sources model 20 002 500-100. The synthesizers inside these Nova sources perform a frequency multiplication of 250 such that the output frequencies of these sources are 2.44 GHz + {8, 9, 10, 11, 12 kHz}. The Nova sources are followed by 33 dB gain power amplifiers and fed to the antennas. Each antenna transmits 30 dBm of RF power. Each combination of transmitter, power amplifier, and its corresponding antenna are associated with one of these frequencies. As can be seen, we have a narrowband measurement system.

A schematic diagram of the remote receiver is shown in Fig. 4. The signals received at the remote station by all the seven receiving antennas are filtered, downconverted, filtered, and *simultaneously* digitized and discrete Fourier transformed in the HP-1342A analog-to-digital (A/D) instrument. The parameters of the discrete Fourier transform were chosen so as to provide a 100-Hz frequency resolution of the baseband signals. A single GPS-controlled Rubidium clock is used to synchronize the local oscillator feeding the mixers and to synchronize the HP-1342A. The output of the HP-1342A contains 300 time matrix samples for every measurement of the narrowband transfer matrix, $\mathbf{G}$. Recall that this matrix contains all the measured transmission coefficients between every possible combination of transmit-receive pair of antennas. Each sample is a time snapshot of $\mathbf{G}$ as opposed to serial time measurement of all the entries in $\mathbf{G}$. From the measured data we derive the average BLAST capacity, C_B, and the number of degrees of freedom, D_F. Compared to the channel coherence time of few seconds for *stationary* remote terminals, the measurement time is negligible. Therefore, our method of measuring G has the advantage that the accuracy of our derived C_B and D_F are not affected by temporal fluctuation of the channel. The A/D voltage sampling rate is 50 K-samples/s. The block size is 500 samples, providing a discrete Fourier transform (DFT) for each matrix element of 200 complex coefficients[2] displayed (software limited to avoid aliasing) at 100-Hz intervals. Entries of $\mathbf{H}$ are simultaneously measured every 0.01 s, which is much less than the channel coherence time. Due to the data saving time to the computer, $\mathbf{H}$ matrices are recorded every 0.1 s. In each measurement run, we save 300 consecutive channel matrices, which takes a total of 30 s. Note that the channel coherence is required only for the measurement of each of the $\mathbf{H}$ matrix rather than the entire data record time.

As can be seen in Fig. 4, the van also had the capability of transmitting, which was useful for antenna alignment and reciprocity checks on the equipment.

III. Measurement System Simulation

In this section, we present our analytical studies to determine the required accuracy for our measurement system. Inherent thermal noise limits the accuracy of the measured results. This thermal noise is incorporated in the signal-to-noise ratio of our measurement system and designated as SNR_m. It is of utmost importance to distinguish between SNR_m, which limits our measurements accuracy, and ρ, the projected average communications system signal to noise ratio, used to obtain C_B and D_F in (1)–(4).

The transfer matrices $\mathbf{G}$, associated with possible propagation environments can vary in nature from fully random independent identically distributed (i.i.d.) Rayleigh matrices, $\mathbf{G_R}$, with the highest nonartificial[3] C_B, to matrices generated by a single dyad, with the lowest C_B. The latter corresponds to either a reflectionless far-field free-space wave propagation, $\mathbf{G_{fs}}$, or a keyhole environment [12], $\mathbf{G_{kh}}$. The corresponding matrices assume the following forms:

$$\mathbf{G_R} = [G_{ij}^R], \quad i = 1,2\ldots 7;\ j = 1,2\ldots 5 \tag{6a}$$

$$\mathbf{G_{fs}} = (1 \quad 1 \quad 1 \quad 1 \quad 1 \quad 1 \quad 1)^{\mathrm{t}} (1 \quad 1 \quad 1 \quad 1 \quad 1) = \left[G_{ij}^{fs}\right] \tag{6b}$$

$$\mathbf{G_{kh}} = (\, G_{r1}^{kh} \quad G_{r2}^{kh} \quad G_{r3}^{kh} \quad G_{r4}^{kh} \quad G_{r5}^{kh} \quad G_{r6}^{kh} \quad G_{r7}^{kh} \,)^t \times (\, G_{t1}^{kh} \quad G_{t2}^{kh} \quad G_{t3}^{kh} \quad G_{t4}^{kh} \quad G_{t5}^{kh} \,) \tag{6c}$$

where all entries in (6a) and (6c) are normally (complex Gaussian) i.i.d. The superscript t designates the transposition operator.

The matrix $\mathbf{G_R}$ is normally and i.i.d. and so is the thermal noise in the measurement receivers. Adding the noise to $\mathbf{G_R}$ results in another matrix with normally i.i.d. elements. Therefore, we do not expect the measurement thermal noise to strongly influence the accuracy of C_B and D_F of (3) and (5). On the other hand, $\mathbf{G}_{\mathrm{fs}}$ and $\mathbf{G}_{\mathrm{kh}}$ are characterized by a single nonzero eigenvalue. A large i.i.d. thermal noise in the receivers could result in a matrix having more than one significant eigenvalue, which would imply erroneously higher values of C_B and D_F.

Fig. 5 shows the calculated D_F of a single sample of a 5×7 $\mathbf{G}_{\mathrm{kh}}$ with 200 different samples of i.i.d. thermal noise representing the measurement system SNR, designated as SNR_m. The range of values of SNR_m is between 5 and 50 dB.

[2]Due to the symmetry in frequency spectrum of the time sequences, only 200 frequency components are used to minimize aliasing.

[3]The highest capacity for an artificial channel is the capacity for a matrix with full rank and equal eigenvalues.

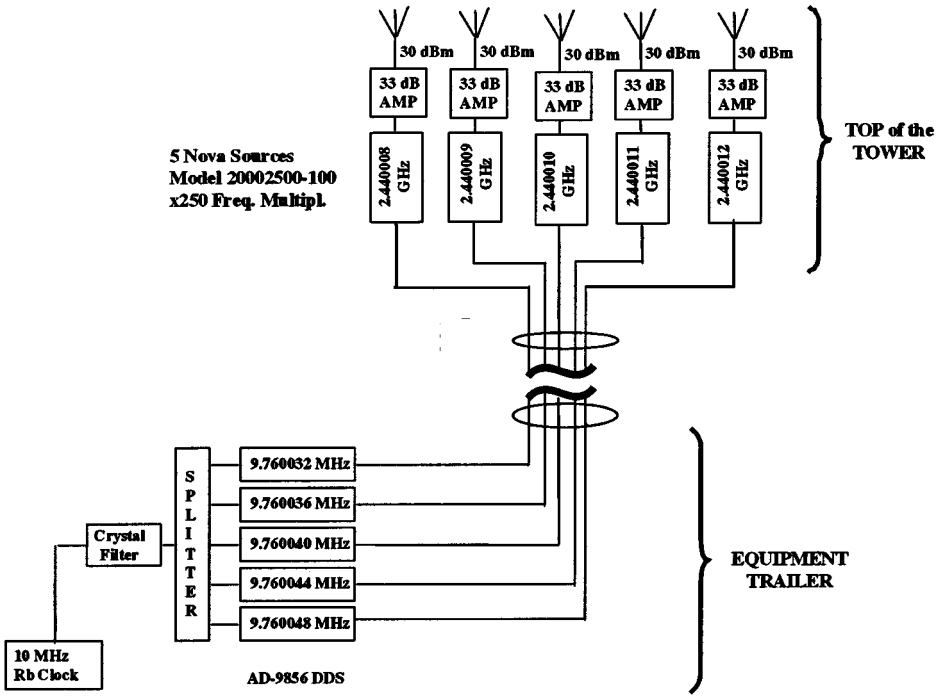

Fig. 3. Schematic diagram of the base station transmitter.

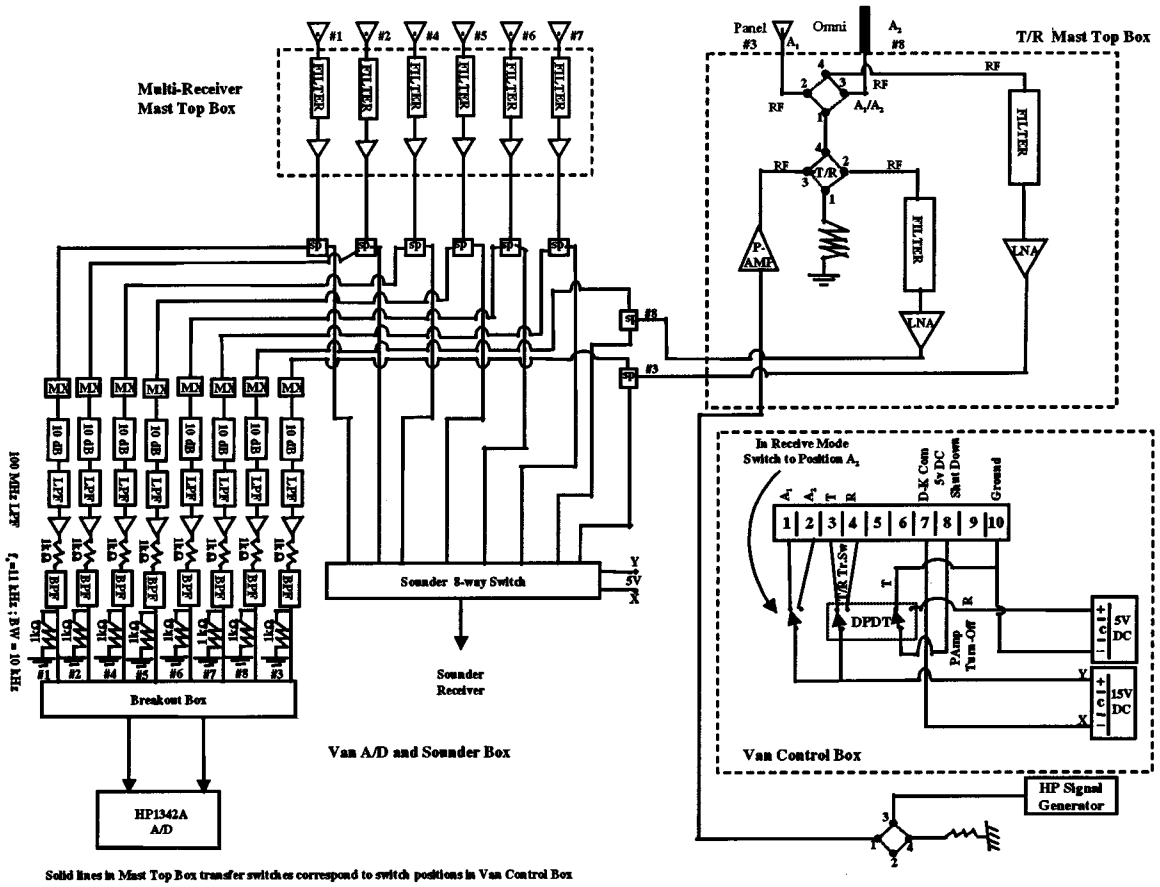

Fig. 4. Schematic diagram of the remote station.

For such a dyadic matrix, $D_F = 1$. At $\mathrm{SNR}_m = 5$ dB, Fig. 5(a), D_F erroneously approaches 5, the value associated with $\mathbf{G}_R$. Even at $\mathrm{SNR}_m = 30$ dB, Fig. 5(b), we note erroneously high values of D_F with an average of 2.82. At $\mathrm{SNR}_m = 50$ dB, D_F attains an average of 1.05 which is close to the correct value of unity. As we shall later see, D_F will be used to assess SNR_m

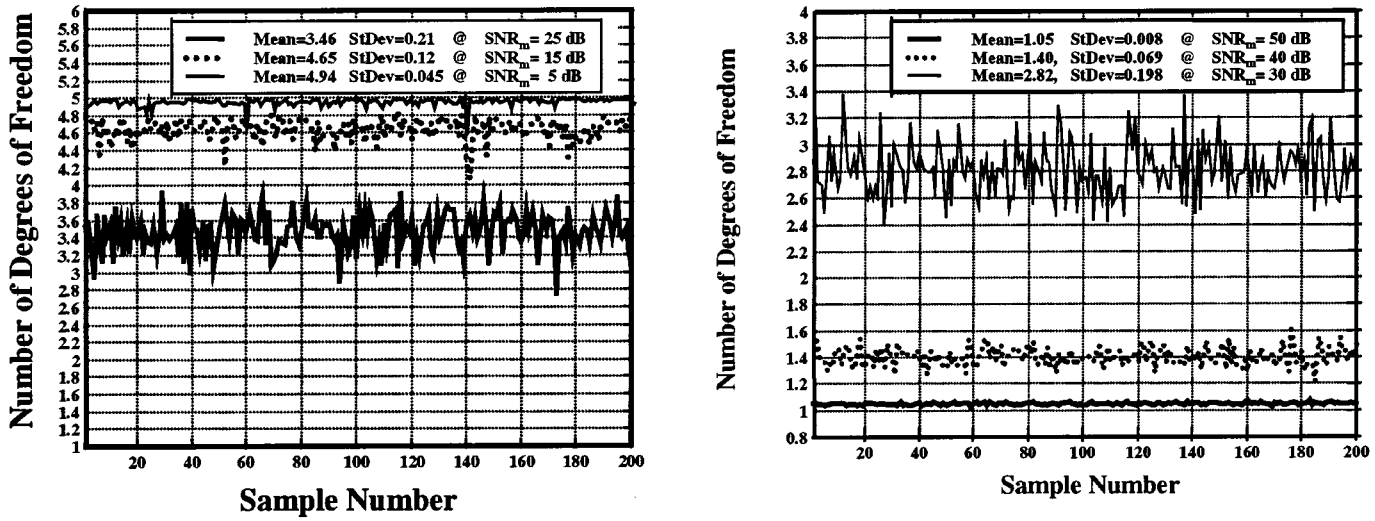

(a) (b)

Fig. 5. Number of degrees of freedom (D_F) of a 5 × 7 random dyadic keyhole versus sample number. (a) SNR_m = 5–25 dB. (b) SNR_m = 30 –50 dB.

in our measurement system. Similar results were exhibited by other samples of $\mathbf{G}_{\mathrm{kh}}$.

In Fig. 6, we demonstrate the corresponding calculated BLAST capacity, C_B, of $\mathbf{G}_{\mathrm{kh}}$ for various values of ρ, the projected communications system SNR. The results are summarized in Table I.

Comparison of C_B obtained with $\mathrm{SNR}_m = 10$ dB, Fig. 6(a), and Table I shows highly erroneous values for the various values of ρ. At $\rho = 5$ dB we have $C_B = 4.53$ for the theoretical versus an erroneous mean $C_B = 6.04$ bits/s/Hz. At higher values, e.g., $\rho = 30$ dB, we have $C_B = 12.77$ for the theoretical versus an erroneous $C_B = 37.38$. This is because the terms containing the erroneous eigenvalues in (3), in conjunction with high ρ value, cannot be neglected anymore. The higher the values of ρ, the more prominent the erroneous eigenvalues become. As SNR_m increases, the values of the erroneous eigenvalues decrease resulting in higher measurement accuracy. At $\mathrm{SNR}_m = 20$ dB, Fig. 6(b), the discrepancy between the theoretical and measured values of C_B is quite small at $\rho = 5$, 10 dB. At $\rho = 20$ and 30 dB, the discrepancy is still large. At $\mathrm{SNR}_m = 30$ dB, Fig. 6(c), the discrepancy is only noticeable at $\rho = 30$ dB. With $\mathrm{SNR}_m = 40$ dB, the calculated C_B is within 1% of theoretical C_B at $\rho = 30$ dB.

IV. Measurement System Calibration

Based upon our simulations we performed the debugging, testing, and calibration of our system. Using a combiner–splitter arrangement, we created an artificial keyhole by connecting the transmitters and receivers back-to-back, Fig. 7(a). We also tested an equal eigenvalue configuration consisting of five independent directly connected transmit to receive channels, Fig. 7(b), with approximately equal gains.

In Fig. 7(a) the five transmitters, having slightly different powers, described by $\{\tau_i\}$, are combined, with coefficients $\{\alpha_i\}$, into a single channel with signal S. A variable attenuator controls SNR_m in the receivers. S is passed through a splitter, downconverted, and filtered. The receiver channels are described by the splitter coefficients $\{\beta_i\}$, amplifier gains $\{r_i\}$, and audio filters $\{g_{ij}\}$. The passive components in this set-up are the splitter, combiner, and the audio filters. The transfer matrix, $\mathbf{G}$, relates the transmit to (7a) receive quantities

$$[R] = [\mathbf{G}][T]. \tag{7a}$$

or in detailed form as (7b), shown at the bottom of the page. The 7×5 $\mathbf{g}$ matrix in (7a) represents the audio filter characteristics of the various receivers. These audio filters are the only components, which are not much wider in bandwidth than the 4-kHz spread in transmitter frequencies. Proper normalization [1] of $\mathbf{G}$ produces the $\mathbf{H}$ matrix used in (1b)–(4). The matrix $\mathbf{G}$ in the direct connection set-up, Fig. 7(b), is a 5×5 diagonal matrix with nearly equal diagonal elements and an additional two rows of zeros corresponding to the terminated receiver ports. While performing the measurements, extreme caution should be exercised in setting the operating range of the HP-1342A A/D converter.

$$\begin{pmatrix} R_1 \\ R_2 \\ R_3 \\ R_4 \\ R_5 \\ R_6 \\ R_7 \end{pmatrix} = \begin{pmatrix} \beta_1 r_1 & & & & \\ & \beta_2 r_2 & & 0 & \\ & & \beta_3 r_3 & & \\ & 0 & & \ddots & \\ & & & & \beta_7 r_7 \end{pmatrix} \begin{pmatrix} g_{11} & \cdots & g_{15} \\ g_{21} & \cdots & g_{25} \\ \vdots & & \vdots \\ g_{71} & \cdots & g_{75} \end{pmatrix} \begin{pmatrix} \alpha_1 \tau_1 & & & & \\ & \alpha_2 \tau_2 & & 0 & \\ & & & \ddots & \\ & 0 & & & \alpha_5 \tau_5 \end{pmatrix} \begin{pmatrix} T_1 \\ T_2 \\ T_3 \\ T_4 \\ T_5 \end{pmatrix} \tag{7b}$$

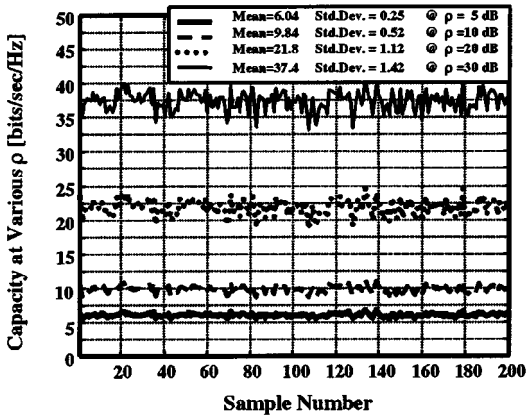

(a)

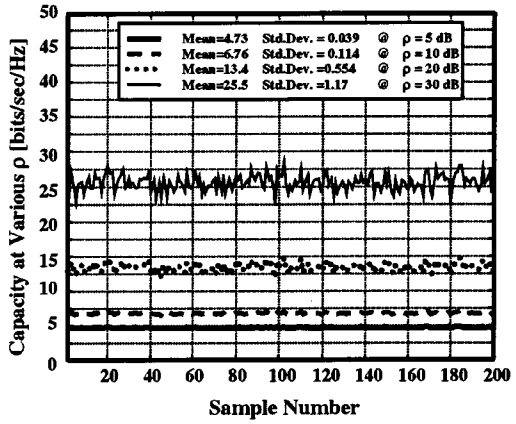

(b)

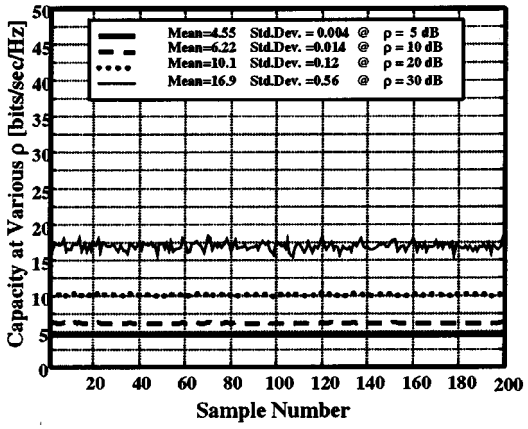

(c)

Fig. 6. BLAST capacity (C_B) of a 5×7 random dyadic keyhole versus sample number. (a) $\mathrm{SNR}_m = 10$ dB. (b) $\mathrm{SNR}_m = 20$ dB. (c) $\mathrm{SNR}_m = 30$ dB.

If the range is set lower than the peaks of the signal to be measured, saturation effects will be injected into the results. This saturation manifests itself in generating nonlinearities and generation of spurious responses that couple from one signal into all the others and causing substantial amplitude fluctuations. When the range is set too high, the resulting lower resolution would produce higher quantization noise.

In our measurements of the artificial keyhole we adjusted the variable attenuator, Fig. 7(a), to provide an input RF power in the range of -125 dBm to -5 dBm at the inputs of the seven RF splitters, *sp* in Fig. 4. The curve labeled signal, in Fig. 8, demonstrates the saturation of the A/D converter, at the maximum A/D converter setting of 20 V, for input powers, at the RF splitters, greater than -30 dBm. The transfer matrices as described by (7a) and (7b), $\{\mathbf{G_j},\ j = -120, \ldots, -5\}$, were measured for each setting of the variable attenuator corresponding to a range of the input power from -125 dBm to -5 dBm in 5-dBm steps. Processing of the matrices, $\{\mathbf{G_j},\ j = -120, \ldots, -5\}$, as outlined above, yielded the degrees of freedom, D_F, and BLAST capacity, C_B, shown by the dashed curves, respectively. Note that dashed D_F curve in the range of -60 dBm to -30 dBm of input power attains a minimum of 1.73. This value deviates from the theoretical value of 1. In tracing the possible sources of this discrepancy, we suspected the audio filters feeding the HP-1342A A/D converter rather than noise or nonlinearities. The phase and amplitude ripple over the audio band may vary from one filter to another, thus causing the discrepancy observed in Fig. 8. In order to ascertain this suspicion, we used a *single* arbitrary time sample of G^S_{-35}, as a reference and divided all the time samples of the measured transfer matrices by it in the following manner:

$$\mathbf{GN_j} = \left[\frac{G_j(k,l)}{G^S_{-35}(k,l)}\right] \tag{8}$$

thus producing a new set of transfer matrices $\mathbf{GN_j}$ in which the audio filters characteristics have, thus, been eliminated. After proper normalization of these new matrices we derived the corrected C_B and D_F shown in Fig. 8 by the solid curves, respectively. Note that this D_F is practically equal to 1 over the range of input power ranging from -65 dBm to -30 dBm. This precludes the system noise and nonlinearities as contributors to the discrepancy observed above. These results coupled with Fig. 5(b) indicate that at -60 dBm input power, $\mathrm{SNR}_m >$ 40 dB. C_B does not seem to be as sensitive a measure as D_F for the measurement accuracy at $\rho = 10$ dB. Between -80 and -5 dBm, the measured error in C_B is under 1%. In the direct connection arrangement, Fig. 7(b), the five channels are uncoupled and approximately equal in strength. To first order in the differences in diagonal elements, it implies $D_F = 5$. Our experimental results, at three measured points, produced this result as shown in Fig. 8 being marked by $\times$.

An alternative keyhole is shown in Fig. 9. In this arrangement, we substituted the combiner of Fig. 7 by free space transmission of the signals. The signal received by a single antenna is split and fed to all the receivers.

TABLE I
BLAST CAPACITIES, C_B [BITS/SEC/HZ], FOR A 5×7 RANDOM DYADIC KEYHOLE AT VARIOUS VALUES OF ρ AND SNR_m. AVERAGED OVER 200 NOISE SAMPLES

ρ [dB]	5	10	20	30
Theoretical C_B	4.53	6.15	9.45	12.77
Calculated C_B with $\mathrm{SNR}_m = 10$ dB	6.04	9.84	21.8	37.4
Calculated C_B with $\mathrm{SNR}_m = 20$ dB	4.73	6.76	13.4	25.5
Calculated C_B with $\mathrm{SNR}_m = 30$ dB	4.55	6.22	10.1	16.9

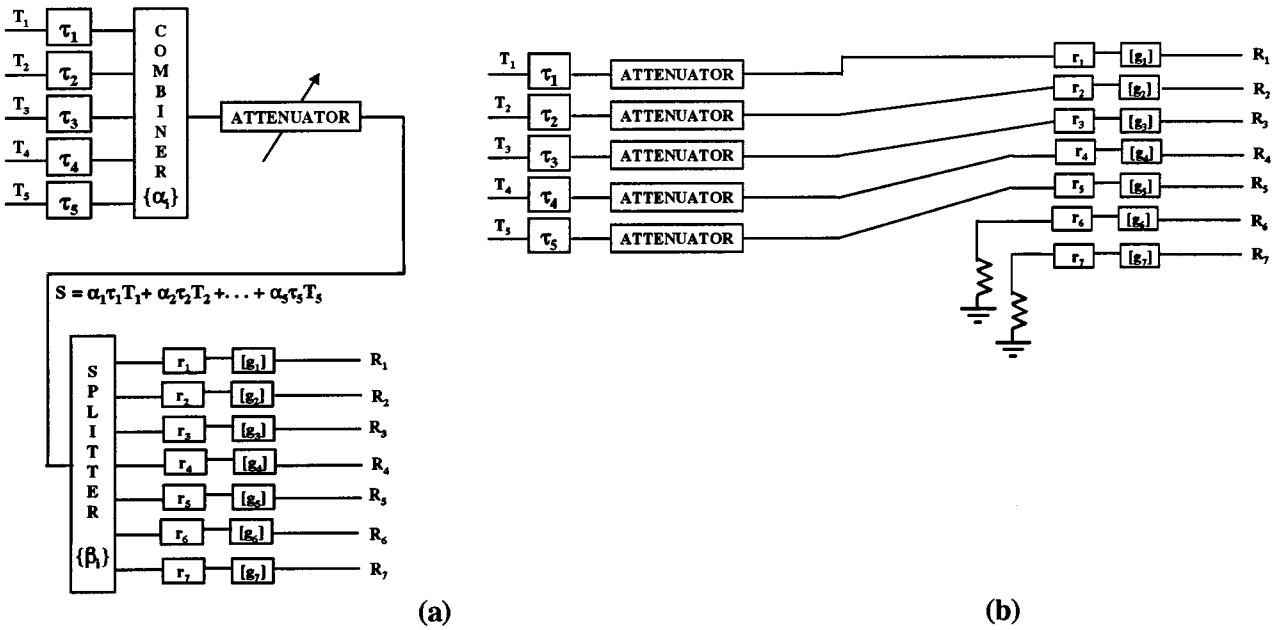

Fig. 7. Initial system calibration tests. (a) Artificial keyhole. (b) Direct connections.

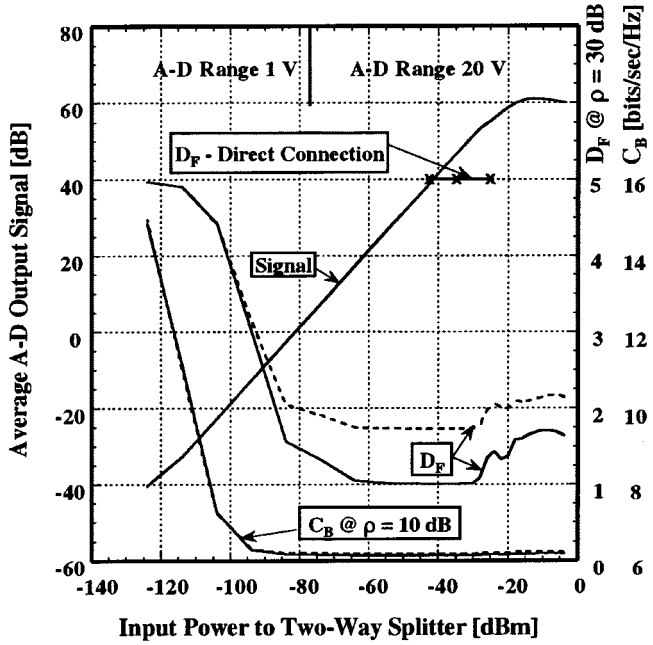

Fig. 8. Measured and corrected C_B and D_F versus power level. Dashed curves are prior to correction. Solid curves are after correction.

The transfer matrix, $\mathbf{G^{kh}}$, of this arrangement is described by the following expression:

$$\mathbf{G^{kh}} = \begin{pmatrix} \beta_1 r_1 & & & \\ & \beta_2 r_2 & & 0 \\ & & \beta_3 r_3 & \\ & 0 & & \ddots \\ & & & \beta_7 r_7 \end{pmatrix} \times \begin{pmatrix} g_{11} & \cdots & g_{15} \\ g_{21} & \cdots & g_{25} \\ \vdots & & \vdots \\ g_{71} & \cdots & g_{75} \end{pmatrix} \begin{pmatrix} \tau_1 & & \\ & \tau_2 & 0 \\ & 0 & \ddots \\ & & \tau_5 \end{pmatrix} \quad (9)$$

where $\{\tau_i\}$ now includes the complex gain from each transmit antenna to the splitter. Measurements were again performed for the same range of input powers as before. The normalization with a single sample from $\mathbf{G_{-40}}$, $\boldsymbol{G^S_{-40}}$, was

$$\mathbf{GN_j} = \left[\frac{G_j(k,l)}{G^S_{-40}(k,l)} \right]. \quad (10)$$

Fig. 10 shows the averaged values of $D_F \pm$ one standard deviation. Note that the measurement noise in the various temporal samples is i.i.d. Therefore, using (10) for all the time samples of the matrix $\mathbf{GN_{-40}}$, does not eliminate the effects of measurement noise. Thus, Fig. 10 combined with our simulation results shown in Fig. 5(b) indicates that SNR_m is above 50 dB over the -55 dBm to -25 dBm range of input power. We also performed on later measurements the normalization indicated in (10) using a three-day-old single sample of $\mathbf{G_{-40}}$. The results are illustrated in Fig. 11 and are consistent with the previous results. At -60 dBm and -20 dBm of input powers, SNR_m is well above 40 dB.

Recall that the simulations shown in Fig. 6 indicated that accurate measurements of C_B could be achieved with $\mathrm{SNR}_m =$ 40 dB. Therefore, for input powers above -60 dBm, the worst measurement error of C_B will be under 1.4% for $\rho \leq 20$ dB.

V. Measurement Procedure

A measurement procedure was established and tested in order to guarantee accuracy in our actual measurement campaign. Based upon our previous testing, we concluded that the characteristics of the passive audio filters do not change with time. On the other hand, the gains of the various active components may vary, and, therefore, have to be calibrated on a daily basis during the campaign.

Fig. 12 depicts the calibration site arrangement. The remote subscriber van is placed at a preset location, 82.3 m away from the base station, and its antennas are raised to 10 m.

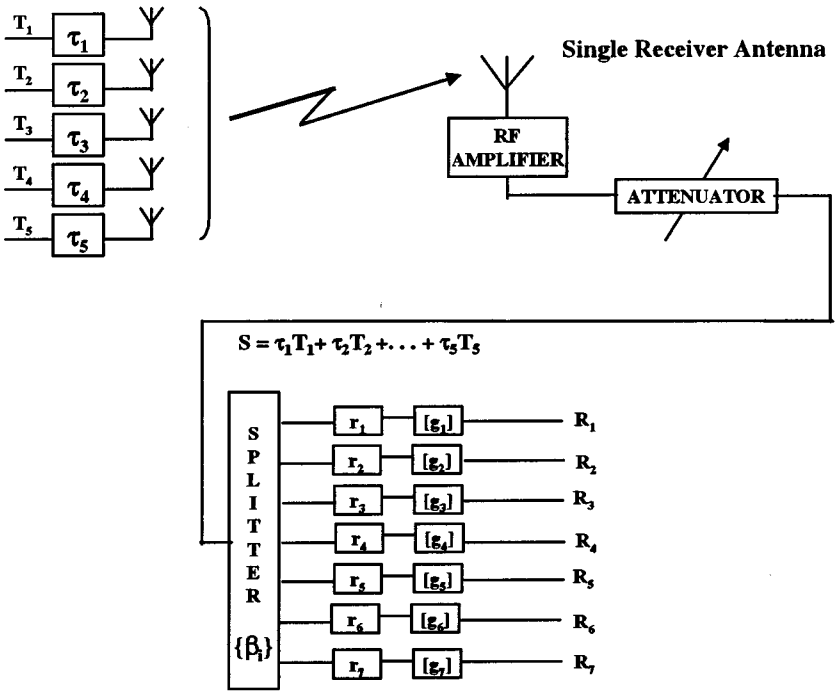

Fig. 9. Free space keyhole.

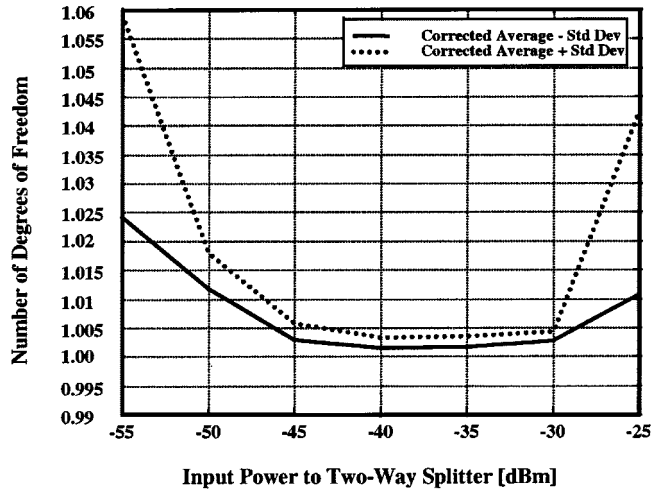

Fig. 10. Averaged number of degrees of freedom $(D_F)\pm$ one standard deviation of $\mathbf{H}^{\dagger}\mathbf{H}$ for 5×7 free space dyadic keyhole versus input power.

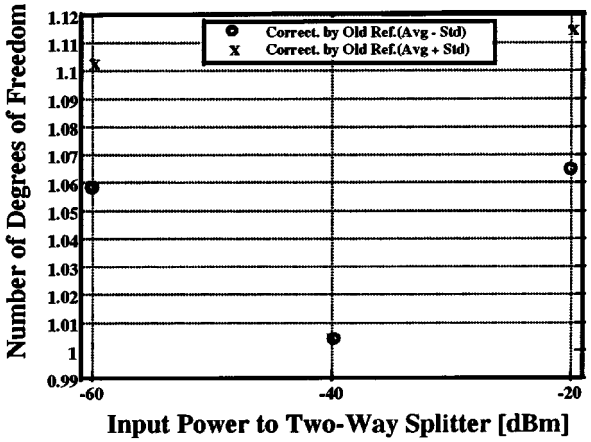

Fig. 11. Averaged number of degrees of freedom $(D_F)\pm$ one standard deviation. 5×7 dyadic keyhole at three values of input power. Old reference sample.

This arrangement, aided by the directivities of the antennas, simulates reflectionless wave propagation. This was verified by moving the remote subscriber antennas up and down and noting no changes in the received signals. This was also verified by calculations of the ground reflections using the radiation pattern of the transmitting and receiving antennas elements. The free space propagation coefficients between the lth transmit and ith receive pair are $v_{il} = \exp(jkd_{il})/d_{il}$. For the arrangement shown in Fig. 12, all d_{il} are nearly identical. The minute differences between the various d_{il} affect only the phases of v_{il}.

Employing the above observations, we arrived at our calibration procedure. We measure the transfer matrix $\mathbf{G_{cal}}$ at the calibration site. The primed diagonal matrices represent the various gains in the transmitting and receiving channels, which could vary from day to day. Using $\boldsymbol{G^{S}_{-40}}$ from (9) and (10), we form

$$\mathbf{G_{cal}} = \begin{pmatrix} r'_1 & & & \\ & r'_2 & 0 & \\ & & r'_3 & \\ & 0 & & \ddots \\ & & & r'_7 \end{pmatrix} \times \begin{pmatrix} v_{11}g_{11} & \cdots & v_{15}g_{15} \\ v_{21}g_{21} & \cdots & v_{25}g_{25} \\ \vdots & & \vdots \\ v_{71}g_{71} & \cdots & v_{75}g_{75} \end{pmatrix} \begin{pmatrix} \tau'_1 & & & \\ & \tau'_2 & 0 & \\ & 0 & \ddots & \\ & & & \tau'_5 \end{pmatrix} \quad (11)$$

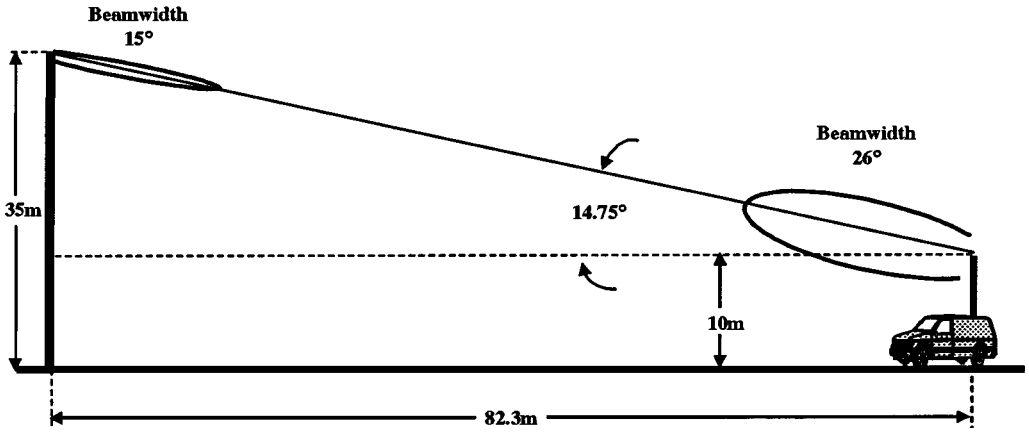

Fig. 12. Daily calibration site arrangement.

a new matrix, $\mathbf{M_{cal}}$, by dividing $\mathbf{G_{cal}}$, element-by-element, by $\boldsymbol{G}^{\boldsymbol{S}}_{\boldsymbol{-40}}$

$$\mathbf{M_{cal}} = \begin{pmatrix} \frac{r_1' v_{11} g_{11} \tau_1'}{\beta_1 r_1 g_{11} \tau_1} & \cdots & \frac{r_1' v_{15} g_{15} \tau_5'}{\beta_1 r_1 g_{15} \tau_5} \\ \vdots & & \vdots \\ \frac{r_7' v_{71} g_{71} \tau_1'}{\beta_7 r_7 g_{71} \tau_1} & \cdots & \frac{r_7' v_{75} g_{75} \tau_5'}{\beta_7 r_7 g_{75} \tau_5} \end{pmatrix}. \quad (12)$$

Note that the filter coefficients, $\{g_{kl}\}$, drop out in (12). Upon taking the absolute value of all the elements of $\mathbf{M_{cal}}$ we obtain the calibration matrix, $\boldsymbol{\kappa}_{\mathbf{cal}}$

$$\boldsymbol{\kappa}_{\mathbf{cal}} = \begin{pmatrix} \left|\frac{r_1' \tau_1'}{\beta_1 r_1 \tau_1}\right| & \cdots & \left|\frac{r_1' \tau_5'}{\beta_1 r_1 \tau_5}\right| \\ \vdots & & \vdots \\ \left|\frac{r_7' \tau_1'}{\beta_7 r_7 \tau_1}\right| & \cdots & \left|\frac{r_7' \tau_5'}{\beta_7 r_7 \tau_5}\right| \end{pmatrix}. \quad (13)$$

Since $|v_{il}| =$ Constant, we set it to unity since it is not going to influence $\mathbf{H}$, [1], [2]. $\boldsymbol{\kappa}_{\mathbf{cal}}$ is obtained prior to the start of daily measurement campaign. It is used to correct for the daily variations as well as indicate if there are any problems in the gains of the receiving or transmitting channels. At every remote subscriber site we measure a temporal set of transfer matrices, $\mathbf{G_{meas}}$.

$$\mathbf{G_{meas}} = \begin{pmatrix} r_1' & & & \\ & r_2' & 0 & \\ & & r_3' & \\ & 0 & \ddots & \\ & & & r_7' \end{pmatrix} \times \begin{pmatrix} c_{11} g_{11} & \cdots & c_{15} g_{15} \\ c_{21} g_{21} & \cdots & c_{25} g_{25} \\ \vdots & & \vdots \\ c_{71} g_{71} & \cdots & c_{75} g_{75} \end{pmatrix} \begin{pmatrix} \tau_1' & & & \\ & \tau_2' & 0 & \\ & 0 & \ddots & \\ & & & \tau_5' \end{pmatrix} \quad (14)$$

where the entries $\{c_{jl}\}$ of the transfer matrix $\mathbf{c}$ represent the propagation coefficients between the lth transmit and jth receive pair of antennas elements. The transfer matrix, $\mathbf{c}$, is utilized to determine the BLAST capacity of the link between the base station and the remote subscriber site. Note that an element-by-element division of $\mathbf{G_{meas}}$ by $\boldsymbol{G}^{\boldsymbol{S}}_{\boldsymbol{-40}}$, yielding $\mathbf{D_{meas}}$, eliminates the audio filter coefficients. Additional element-by-element division of $\mathbf{D_{meas}}$ by $\boldsymbol{\kappa}_{\mathbf{cal}}$ yields (15) at the bottom of the page, where $\exp(j\phi_i) = (r_i'/|r_i'|)(|\beta_i r_i|/\beta_i r_i|)$ and $\exp(j\theta_k) = (\tau_k'/|\tau_k'|)(|\tau_k|/\tau_k)$. The two diagonal matrices in (15) are unitary and, therefore, the eigenvalues of $\mathbf{C}^{\dagger}\mathbf{C}$ are the same as $\mathbf{c}^{\dagger}\mathbf{c}$. After the normalization of $\mathbf{C}$ [1], [2], we derive the corresponding $\mathbf{H}$ matrix and use (1b) to obtain the BLAST capacity. A detailed comparison of the measured and theoretical BLAST capacity values for this system over a controlled propagation environment is presented in [14].

VI. Initial Results

A. Measurements

So far, our measurement campaign included 16 locations surrounding Crawford Hill at distances of up to 10.3 km. Measurements were performed for remote subscriber's antenna heights of 5 and 10 m. Following our measurement procedure described above we obtained the average BLAST capacities, C_B, averaged over 300 temporal samples taken during a 30 s time interval.

Fig. 13 illustrates some of our results. Note that our measurements results are bounded between the fully random Rayleigh i.i.d. transfer matrices case and the 5×7 keyhole case. This is as it should be and it adds credibility to the quality of our measurements. The 1×1 keyhole case corresponds to a single receive and a single transmit antennas case. As can be seen, there are some good sites with BLAST potential where C_B is close to the Rayleigh i.i.d. case distribution curve. Unfortunately some

$$\mathbf{C} = \begin{pmatrix} \exp(j\phi_1) & & & \\ & \exp(j\phi_2) & 0 & \\ & 0 & \ddots & \\ & & & \exp(j\phi_7) \end{pmatrix} \begin{pmatrix} c_{11} & \cdots & c_{15} \\ c_{21} & \cdots & c_{25} \\ \vdots & & \vdots \\ c_{71} & \cdots & c_{75} \end{pmatrix} \begin{pmatrix} \exp(j\theta_1) & & & \\ & \exp(j\theta_2) & 0 & \\ & 0 & \ddots & \\ & & & \exp(j\theta_5) \end{pmatrix} \quad (15)$$

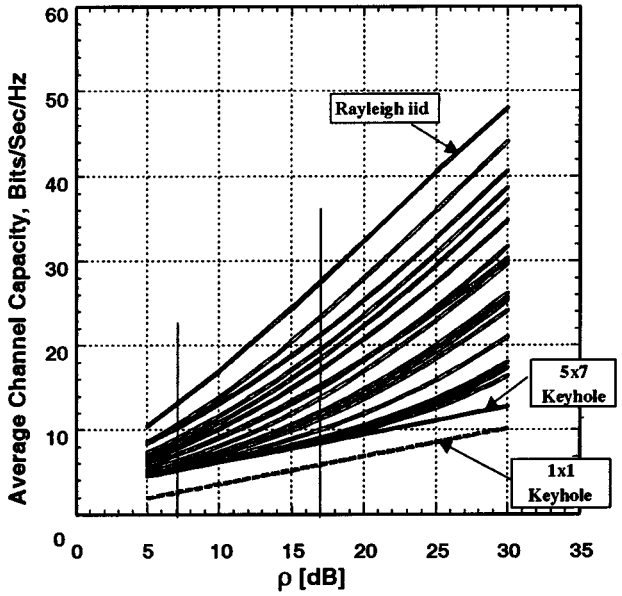

Fig. 13. Average channel capacity, C_B, versus ρ. Derived from measurements at 16 locations. Remote subscriber height 10 m.

bad sites also exist, where C_B is closer to the 5×7 keyhole case curve. Cumulative distributions of the above data were derived for the commonly used ρ of 7 and 17 dB. These are shown in Fig. 14. For $\rho = 7$ dB, Fig. 14(a), $C_B \geq 8.2$ bits/s/Hz at 20% of the locations while $C_B \geq 5.8$ bits/s/Hz at 50% of the locations. These results do not demonstrate a large BLAST capacity advantage over the 5.2 bits/s/Hz channel capacity of a 5×7 keyhole. The corresponding average Rayleigh i.i.d. channel capacity is 13 bits/s/Hz for $\rho = 7$ dB. A higher BLAST advantage can be seen at $\rho = 17$ dB, Fig. 14(b). Here, 20% of the location have $C_B \geq 18$ bits/s/Hz while 50% of the locations have $C_B \geq 12$ bits/s/Hz. The corresponding channel capacity of a 5×7 keyhole is 8.46 bits/s/Hz.

At 5 m antenna height at the remote subscribers' sites the values of C_B were slightly higher than the corresponding values at 10 m antenna height. This indicates an additional environmental scattering at the lower heights.

B. Effects of Sideband Noise

Sideband noise is generated by the phase noise inherent in each transmitting frequency source. At the receivers, we associate each tone, with its narrow bandwidth with a particular transmitter antenna. Since portions of the sideband noise transmitted from any four antennas couple into the band associated with the fifth antenna, measurement errors of the transfer matrix $\mathbf{G}$ are introduced.

Prior to the start of our measurement campaign, the above sideband noise power in any given band contributed by four transmitting sources was 32 dB below the desired power transmitted from the fifth source. At the end of our campaign, the measured sideband noise power increased to 20 dB below the desired transmitted power. To assess the degradation in the measurement accuracy due to sideband noise we relate the actually

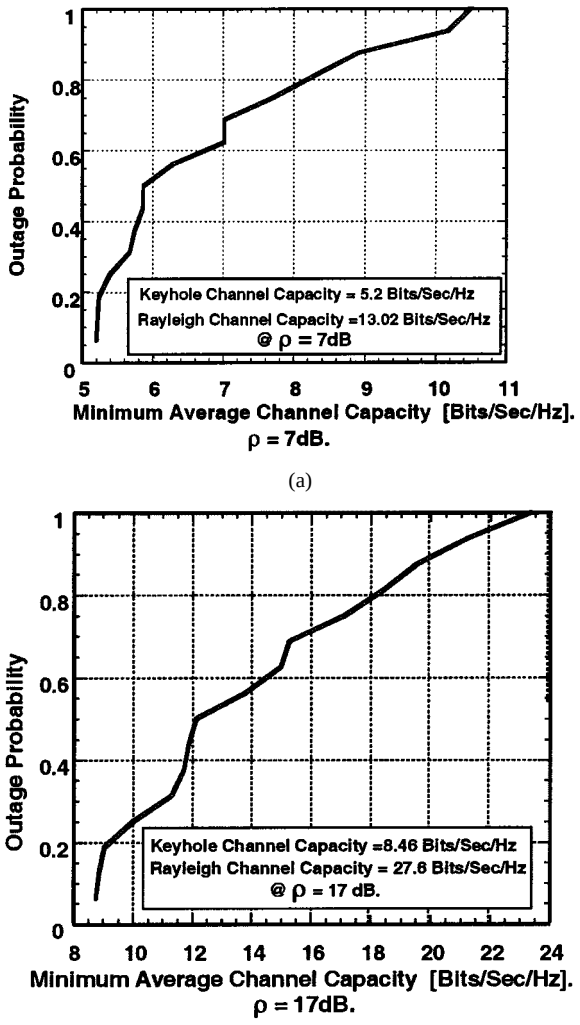

Fig. 14. Cumulative distribution of the capacity for 16 locations, 10 m remote height. (a) $\rho = 7$ dB. (b) $\rho = 17$ dB.

transmitted signals vector $[T_a]$ to the pure desired tones $[T]$ via the following sideband noise matrix $\boldsymbol{\gamma}$

$$\begin{pmatrix} T_{a1} \\ T_{a2} \\ T_{a3} \\ T_{a4} \\ T_{a5} \end{pmatrix} = \begin{pmatrix} 1 & & & & \\ & 1 & & \gamma_{i \neq j} & \\ & & 1 & & \\ & \gamma_{i \neq j} & & 1 & \\ & & & & 1 \end{pmatrix} \begin{pmatrix} T_1 \\ T_2 \\ T_3 \\ T_4 \\ T_5 \end{pmatrix}; \quad \gamma_{i \neq j} \text{ are normally i.i.d.} \tag{16}$$

The BLAST capacity, C_{Bsb}, with the effects of the sideband noise is obtained from the products $\boldsymbol{G}_{-40}^{\boldsymbol{S}}\boldsymbol{\gamma}$, $\mathbf{G}_{\mathbf{cal}}\boldsymbol{\gamma}$ and the various temporal samples of $\mathbf{G}_{\mathbf{meas}}\boldsymbol{\gamma}$. Each one of the previous matrices is multiplied by an independent sample of $\boldsymbol{\gamma}$. This is because the sideband noise is contributed by a continuous spectrum across the 100-Hz bandwidth of the receiver DFT for each transmitter. This produces a randomly varying phasor, independent from measurement to measurement. Employing the previously described procedures and the measured data (assumed to be accurate), we evaluate C_{Bsb} for different standard deviations of $\gamma_{i \neq j}$. We picked three measured locations with low, medium,

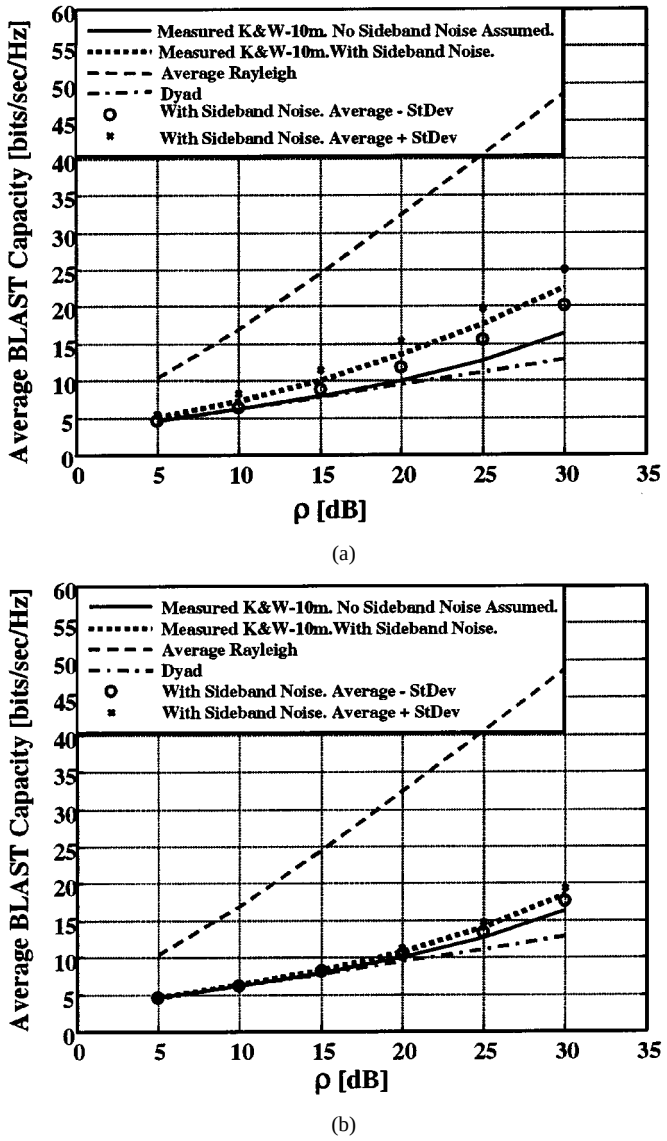

Fig. 15. Average BLAST capacities versus ρ. (a) 10-dB signal-to-sideband noise ratio. (b) 20-dB signal-to-sideband noise ratio.

and high C_B. Highest inaccuracies due to sideband noise occurred at the lower value of C_B, closer to the dyad. These effects are demonstrated in Fig. 15.

Based upon the simulation we conclude that the effects of the sideband noise in our measurements are negligible.

C. Straw-Man System

The measured results were used to examine a hypothetical system serving our measured sites with a 30-kHz channel bandwidth, a 10-dB receiver noise figure, and negligible interference. Propagation path losses are accounted for in the link budgets. The propagation losses were calculated as decibel sums of two terms. The free space path loss between the base station antenna ports and mobile antenna ports at the calibration site is PL_1. The measured path loss between the remote at the calibration site to the remote subscriber site is PL_2

$$\mathrm{PL}_1 = 20\mathrm{Log}_{10}\left(\frac{4\pi d_{\mathrm{fs}}}{\lambda}\right) - (g_t - g_r) \qquad (17a)$$

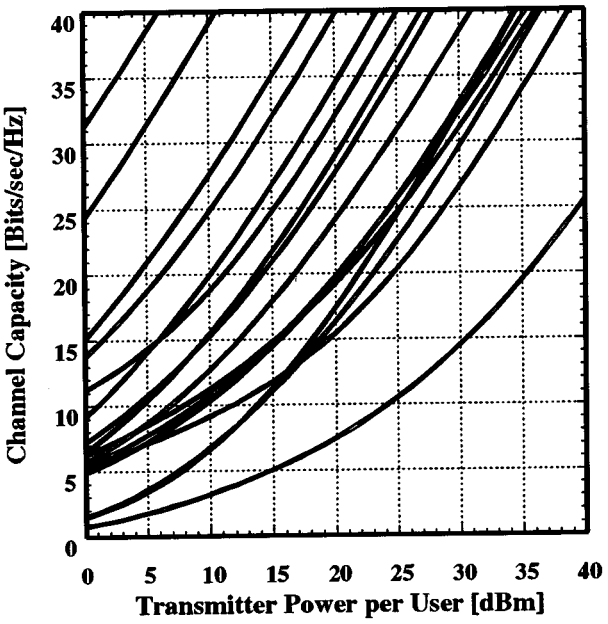

Fig. 16. Average BLAST capacity, C_B, of the measured sites versus subscriber power.

where g_t and g_r are the transmit and receive antenna gains, expressed in decibels, respectively. The distance between the base station and mobile antennas at the calibration site is d_{fs}

$$\mathrm{PL}_2 = 10\mathrm{Log}_{10}\left(\|\boldsymbol{G}_{\mathbf{cal}}\|^2\right) - 10\mathrm{Log}_{10}\left(\|\boldsymbol{G}_{\mathbf{meas}}\|^2\right). \qquad (17b)$$

With $\|X\|^2 = \sum_{\forall i,k} \overline{|X_{i,k}|^2}/(N_T N_R)$, the bar designates time average over the measured samples. X stands for either $\boldsymbol{G}_{\mathbf{meas}}$ or $\boldsymbol{G}_{\mathbf{cal}}$. The measured power at the remote antenna, W_{rec}, is

$$W_{\mathrm{rec}} = W_T - \mathrm{PL}_1 - \mathrm{PL}_2 \qquad (18)$$

where W_T is the transmitted power. Based upon the above equations, ρ was derived for the various sites and used in (1b) to obtain the average values of C_B for the measured remote subscriber sites as a function of the transmitted power. Fig. 16 displays the results. For transmit power of 20 dBm, the range of values of C_B falls between 7 and over 40 bits/s/Hz. Except for one subscriber site, $C_B \geq 15$ bits/s/Hz at all the other 15 sites. To highlight the BLAST advantage we show in Fig. 17 the capacity of focused directive beam (keyholes) channels at the same locations. In these cases the corresponding ρ is increased from its previous values by the gain of the focused beam antenna at the transmitter. For transmit power of 20 dBm, the range of values of C_B falls between 8.5 and 23.5 bits/s/Hz. At only five subscriber sites, $C_B \geq 15$ bits/s/Hz. The focused directive beam results assume that the transmitter knows where to aim and that scattering does not significantly degrade the directivity of the focused beam. Note that the BLAST capacity formula (1b) assumes a blind transmitter, except the remote should lie within the broad antenna element pattern.

Cumulative distributions of the capacities of the BLAST and focused directive beam cases are shown in Figs. 18 and 19, respectively. BLAST capacities of $C_B \geq 38$ bits/s/Hz at 20% of

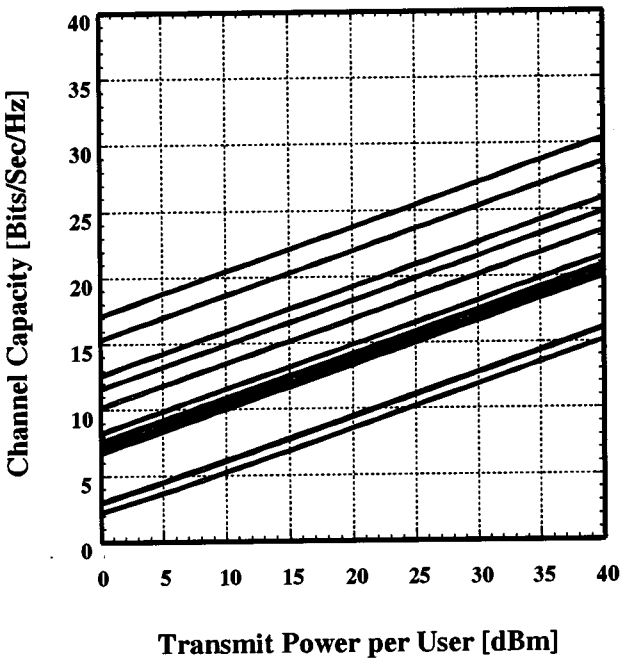

Fig. 17. Extrapolated capacity for focused directive beam (keyholes) in the measured sites versus subscriber power.

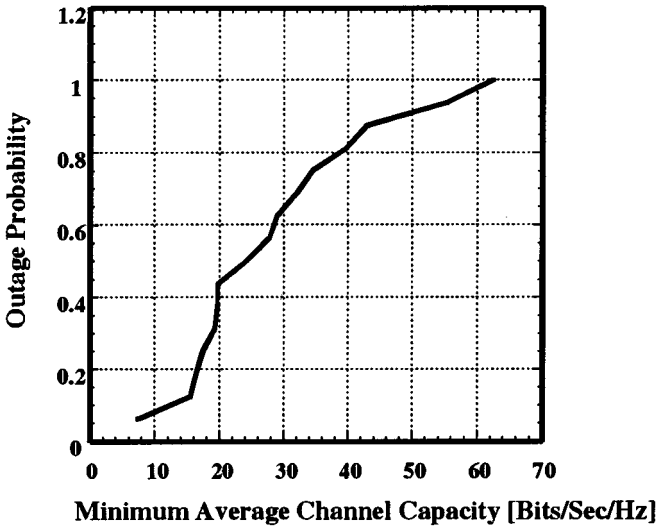

Fig. 18. Cumulative distribution of BLAST capacity for 16 locations. Transmitter power per user = 20 dBm, 10 m remote height.

the locations and $C_B \geq 24$ bits/s/Hz at 50% of the locations are feasible. The corresponding capacities, C, of the focused directive beam cases are $C \geq 18$ bits/s/Hz at 20% of the locations and $C \geq 14$ bits/s/Hz at 50% of the locations. The BLAST advantage is quite noticeable.

VII. Conclusion

A measurement campaign was undertaken to assess the BLAST gains in spectral efficiency in the suburban outdoor environment for stationary subscribers. The measurements employed five transmitting and seven receiving directive antennas to better control interference from adjacent

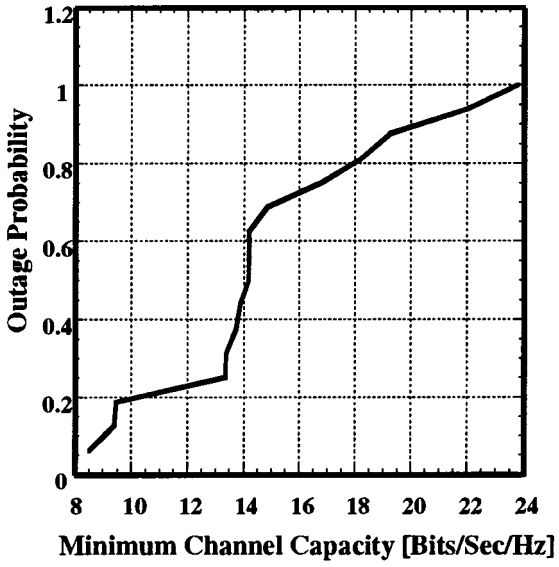

Fig. 19. Cumulative distribution of capacity for 16 locations with focused directive beam. Transmitter power per user = 20 dBm, 10 m remote height.

cells. The measurements were performed over a narrow band at 2.44 GHz. Simulation studies have shown that at $\mathrm{SNR}_m = 20$ dB, the discrepancy between the theoretical and measured values of the BLAST capacity of a keyhole is quite small at $\rho = 5$, 10 dB. Please note that we use SNR_m and ρ to represent *measurement* SNR and the intended communications *system* SNR, respectively. At $\rho = 20$ and 30 dB, the discrepancy is appreciable. At $\mathrm{SNR}_m = 30$ dB, the discrepancy is only noticeable at $\rho = 30$ dB. With $\mathrm{SNR}_m = 40$ dB, we reach high enough accuracy even for $\rho = 30$ dB. We present our accurate calibration methods devised to test our system prior and during our campaign, to ensure SNR_m above 40 dB.

Measurements were performed at 16 locations with remote subscriber antenna heights of 5 and 10 m. We present here the measured results at 10 m. The BLAST capacities, C_B, associated with the various locations, are bounded between the capacities of keyhole and Rayleigh i.i.d. H matrices. Cumulative distributions were derived for the commonly used ρ's of 7 and 17 dB. At $\rho = 7$ dB, at 20% of the locations $C_B \geq 8.2$ bits/s/Hz while for 50% of the locations $C_B \geq 5.8$ bits/s/Hz. These results do not demonstrate a large BLAST capacity advantage over the keyhole channel capacity of 5.2 bits/s/Hz. A Rayleigh i.i.d. channel average capacity is 13 bits/s/Hz. A higher BLAST advantage can be seen at $\rho = 17$ dB. In this case, 20% of the location have $C_B \geq 18$ bits/s/Hz while 50% of the locations have $C_B \geq 12$ bits/s/Hz. The corresponding keyhole channel capacity is 8.46 bits/s/Hz. At 5 m height of the remote subscribers' antennas, the values of C_B were *slightly* higher than the corresponding values at 10 m antenna height. This indicates some additional environmental scattering at the lower heights. The BLAST advantage in an extrapolated straw-man system serving our measured sites, with 30-kHz channel bandwidth and 10-dB receiver noise figure, was demonstrated. BLAST capacities of $C_B \geq 38$ bits/s/Hz at 20% of the locations and $C_B \geq 24$ bits/s/Hz at 50% of the locations are feasible, for reasonable link parameters and negligible interference.

REFERENCES

[1] G. J. Foschini, "Layered space-time architecture for wireless communication in a fading environment when using multiple antennas," *Bell Labs Tech. J.*, vol. 1, no. 2, pp. 41–59, 1996.

[2] G. J. Foschini and M. J. Gans, "On limits of wireless communications in a fading environment when using multiple antennas," in *Wireless Pers. Commun.*. New York: Kluwer, 1998, vol. 6, pp. 311–335.

[3] R. B. Ertel, P. Cardieri, K. W. Sowerby, T. S. Rappaport, and J. H. Reed, "Overview of spatial channel models for antenna array communication systems," *IEEE Pers. Commun. Mag.*, pp. 10–22, Feb. 1998.

[4] K. I. Pedersen, J. B. Andersen, J. P. Kermoal, and P. Modensen, "A stochastic multiple-input–multiple-output radio channel model for evaluation of space-time coding algorithms," in *Proc. IEEE VTC-2000*, sec. 3.1.4.3, Boston, MA, Sept. 24–28, 2000.

[5] J. P. Kermoal, L. Schumacher, P. E. Mogensen, and K. I. Pedersen, "Experimental investigation of correlation properties of MIMO radio channels for indoor picocell scenarios," in *Proc. IEEE VTC-2000*, sec. 2.1.2.3, Boston, MA, Sept. 24–28, 2000.

[6] M. Stege, J. Jelitto, M. Bronzel, and G. Fettweis, "A multiple input-multiple output channel model for simulation of TX and RX diversity wireless systems," in *Proc. IEEE VTC-2000*, sec. 3.1.2.4, Boston, MA, Sept. 24–28, 2000.

[7] D. O. NcBanaram, N. A. Beach, P. Karlsson, and P. N. Fletcher, "Initial characterization of MIMO channels for space-time communication," in *Proc. IEEE VTC-2000*, sec. 3.4.1.4, Boston, MA, Sept. 24–28, 2000.

[8] C. C. Martin, J. H. Winters, and N. R. Sollenberger, "Multiple-input multiple-output (MIMO) radio channel measurements," in *Proc. IEEE VTC-2000*, Boston, MA, Sept. 24–28, 2000.

[9] J. P. Kermoal, P. E. Mogensen, S. H. Jensen, J. B. Andersen, F. Frederiksen, T. B. Sorensen, and K. I. Pedersen, "Experimental investigation of multipath richness for multi-element transmit and receive antenna arrays," in *Proc. IEEE VTC'2000*, May 2000.

[10] G. D. Golden, G. J. Foschini, R. A. Valenzuela, and P. W. Wolniansky, "Detection algorithm and initial laboratory results using V-blast space-time communication architecture," *Electron. Lett.*, vol. 35, pp. 14–16, Jan. 1999.

[11] P. W. Wolniansky, G. J. Foschini, G. D. Golden, and R. A. Valenzuela, "V-BLAST: An architecture for realizing very high data rates over the rich-scattering wireless channel," in *Proc. IEEE ISSSE-98*, Pisa, Italy, Sept. 30, 1998.

[12] D. Chizhik, G. J. Foschini, and R. A. Valenzuela, "Capacities of multi-element transmit and receive antennas: Correlations and keyholes," *Electron. Lett.*, vol. 36, pp. 1099–1100, June 2000.

[13] D.-S. Shiu, G. J. Foschini, M. J. Gans, and J. M. Kahn, "Fading correlation and its effect on the capacity of multielement antenna systems," *IEEE Trans. Commun.*, vol. 48, pp. 502–513, Mar. 2000.

[14] H. Xu, M. J. Gans, N. Amitay, and R. A. Valenzuela, "Experimental verification of MTMR system capacity in a controlled propagation environment," *IEE Electron. Lett.*, vol. 37, pp. 936–937, July 2001.

[15] D. Gesbert, H. Bolcskei, D. Gore, and A. Paulraj, "MIMO wireless channels: Capacity and performance prediction," in *IEEE Globecom 2000*, San Francisco, CA, Nov.–Dec. 27–1, 2000.

Michael J. Gans (M'84–SM'84–SM'91–F'93) received the Ph.D. degree in electrical engineering from the University of California, Berkeley in 1965.

He is on the staff of the Wireless Communications Research Department at Bell Laboratories, Holmdel, NJ. He has been at Bell Laboratories since 1966. His primary technical areas include mobile radio, antennas, satellites, fiber optics, and infrared communications.

Noach Amitay (M'60–SM'76–F'83–LF'96) was born in Tel-Aviv, Israel, on April 30, 1930. He received the B.Sc. and Dipl. Ing. degrees in electrical engineering from Technion, Israel Institute of Technology, in 1953 and 1954, and M.Sc. and Ph.D. degrees in electrical engineering from Carnegie Institute of Technology, Pittsburgh, PA, in 1957 and 1960, respectively.

From 1954 to 1956, he directed the Electronic Measuring and Aligning Instruments Department of the Signal Corps. Defense Army of Israel. He was a Research Assistant in 1957, a Project Engineer in 1958, and an Instructor in 1959, all at Carnegie Institute of Technology. He served as a consultant on electronic instrumentation for Magnetics, Inc., Butler, PA, from 1957 to 1958 and from 1960 to 1961. From 1960 to 1962, he was an Assistant Professor in the department of Electrical Engineering, Carnegie Institute of Technology, and a part-time employee of the New Products Laboratory of Westinghouse Electric Corporation, Pittsburgh, PA. He joined Bell Telephones Laboratories, Inc., Whippany, NJ, in 1962. In Whippany he conducted research in phased array radar and communication antennas, electromagnetic theory and numerical methods and analysis. After relocating to Bell Laboratories in Holmdel, NJ, he has been involved in studies of satellite communications antennas, digital radio communications, lightwave networks, and personal communications systems. In 1996, he retired as a Distinguished Member of the Technical Staff from the Wireless Communications Systems Department of AT&T Bell Laboratories. At present, he is a president of Amitay Associates, LLC, Holmdel, NJ.

Yu Shuan (Albert) Yeh (S'64–M'66–SM'81–F'84) received the B.S. degree in electrical engineering from National Taiwan University in 1961 and the M.S. and Ph.D. degrees from the University of California, Berkeley, in 1964 and 1966, respectively.

After a one-year stay at Harvard University, Cambridge MA, he joined AT&T Bell Laboratories in 1967 until he resigned in 1987 to pursue his own investment interests. From 1988 to 2000, he was a part-time consultant for Bell Laboratories (now a part of Lucent Technologies), Holmdel, NJ. Throughout his career, he was engaged in research on digital communication satellites, digital radio, packet switching, and mobile communications. He has 25 U.S. patents.

Dr. Yeh received two Best Paper Awards from IEEE Transactions.

Hao Xu (S'96–M'00) was born in Wuhan, China, on February 28, 1971. He received the B.S. and M.S. degrees from Moscow Power Engineering Institute and Technical University, Moscow, Russia in 1994 and 1996, respectively. From 1996 to 2000, he worked in Mobile and Portable Radio Research Group (MPRG) at Virginia Polytechnic Institute and State University for his Ph.D. His doctoral research focused on radio wave propagation in 5.85 GHz, 38 GHz and 60 GHz for National Information Infrastructure (NII), Local Multipoint Distribution Systems (LMDS) and Next Generation Internet (NGI) applications.

After receiving the Ph.D. degree in 2000, he joined the Wireless Communications Research Department at Bell Laboratories, Crawford Hill, NJ. His current research includes MIMO channel measurements, modeling, and standardization for third-generation wireless systems. His research interests also include adaptive antenna techniques and advanced receiver design. He has over 20 publications.

Dr. Xu received the IEEE Communications Society Stephen O. Rice Prize Paper Award in 1999. He is a member of Eta Kappa Nu and Sigma Xi Scientific Research Society.

T. C. Damen received the engineering degree from the University of Eindhoven, The Netherlands, and the physics degree from New York University.

He joined Bell Laboratories in 1958 and retired in 2000. He has made numerous contributions in the fields of physics and electrical engineering. He has a total of 161 publications.

Reinaldo A. Valenzuela (M'85–SM'89–F'99) received the B.S. degree from the University of Chile and the Ph.D. degree from the Imperial College of Science and Technology of the University of London, U.K. His doctoral work introduced novel digital filters for transmultiplexers.

At Bell Laboratories, Holmdel, NJ, he studied indoor microwave propagation and modeling, packet reservation multiple access for wireless systems and optical WDM networks. He was Manager, Voice Research Dept., at Motorola Codex, involved in the implementation integrated voice and data packet systems. On returning to Bell Laboratories, he led a multidisciplinary team to create a software tool for Wireless System Engineering (WiSE), now in widespread use at Lucent Technologies. He received the Distinguished Member of Technical Staff award and is now Director of the Wireless Communications Research Department. He is interested in microwave propagation measurements and models, third generation wireless systems, and achieving high capacities employing transmit and receive antenna arrays. He has published over 60 papers and has ten patents.

Dr. Valenzuela received the Distinguished Member of Technical Staff award from Lucent Technologies, Bell Labs Innovations.

Theodore Sizer (M'93) received the B.A. degree in physics and astromony *magna cum laude* from Amherst College, Amherst, MA, in 1979 and the M.S. and Ph.D. degrees from the Institute of Optics, University of Rochester, Rochester, NY, in 1980 and 1985, respectively.

He is a Distinguished Member of Technical Staff in the Wireless Technology Research Department of Bell Laboratories, Holmdel, NJ. During his tenure at Bell, he has performed research in wired and wireless home networking, fixed wireless loop systems, video watermarking technologies, optical computing and switching systems, and high power laser design. Currently, he is focusing his efforts in two areas: the use of antenna arrays for access applications and Bluetooth. He is a member of the technical team in Lucent's role as a promoter in the Bluetooth Special Interest Group (SIG). His responsibilities in the SIG include being Chair of the Coexistence Working Group. He is the author of 34 patents, 16 patents pending, and over 50 refereed publications.

R. Storz, photograph and biography not available at the time of publication.

D. Taylor, photograph and biography not available at the time of publication.

W. M. MacDonald received the B.S. degree in physics from The University of Notre Dame, Notre Dame, IN, in 1979, and the M.S. and Ph.D. degrees in physics from the University of Illinois, Urbana-Champaign, in 1980 and 1984, respectively.

He joined the research staff at AT&T Bell Laboratories, Murray Hill, NJ, in 1984. He has worked on optical communications as well as wireless communications.

Cuong Tran received the B.S. and M.S. degrees in electrical engineering from New Jersey Institute of Technology.

He is a member of High-Speed Circuits and Systems Research department at Bell Laboratories, Holmdel, NJ. He has designed antennas for phased array antenna systems and designed RF and microwave packages and systems for wireless applications. Currently, he is working on direct conversion transceiver for 3G systems.

Andrew Adamiecki was born in Kozieglowy, Poland in 1955. He received the B.S. and M.S. degrees in electrical engineering from the Silesian Technical University, Poland, in 1981 and 1983, respectively.

From 1986 to 1991, he was a Senior RF-Communications Engineer with Ademco, a Division of Pittway Corporation, Syosset, NY working on Direct Sequence Spread Spectrum techniques for commercial security system application. In 1991, he joined AT&T Consumer Product Division working on cellular phones architectures and design for TDMA, CDMA, and GSM standards. He is now a Member of Technical Staff in the Photonics Research Department at Bell Labs Lucent Technologies, Holmdel, NJ. His current work includes microwave and high speed electronics circuit and subsystems design, development, and analysis.